Photoreactions in the Gas-Phase Complexes of $Mg^{\bullet+}$−Dioxanes

Haichuan Liu, Yihua Hu, and Shihe Yang*

Department of Chemistry, The Hong Kong University of Science and Technology, Clear Water Bay, Kowloon, Hong Kong, China

Wenyue Guo,* Qingtao Fu, and Ling Wang

College of Physics Science and Technology, China University of Petroleum, Dongying, Shandong 257061, China

Received: January 1, 2006; In Final Form: February 10, 2006

Photoreactions in the gas-phase complexes $Mg^{\bullet+}$(1,4-dioxane) (**1**) and $Mg^{\bullet+}$(1,3-dioxane) (**1M**) have been examined in the wavelength region of 230−440 nm. Photoproduct assignments are facilitated with the help of deuterium substitution experiments. The main energy relaxation channel for both photoexcited complexes is the evaporation of $Mg^{\bullet+}$. Also observed from **1** are rich photoproducts with *m*/*z* 28, 41, 54−58, 67, 69, and 88; the most abundant one at *m*/*z* 54 is designated to $Mg^{\bullet+}(O{=}CH_2)$. In marked contrast, the photolysis of **1M** yields only $Mg^{\bullet+}(O{=}CH_2)$ other than $Mg^{\bullet+}$. Density functional calculations are performed to obtain optimized geometries and potential energy surfaces of **1** and **1M**. Although $Mg^{\bullet+}$(*chair*-1,4-$C_4H_8O_2$) (**1a**) and $Mg^{\bullet+}$(*boat*-1,4-$C_4H_8O_2$) (**1b**) are comparable in energy, the much better agreement of the experimental action spectrum of $Mg^{\bullet+}$(1,4-$C_4H_8O_2$) with the calculated absorption spectrum of **1a** than with that of **1b** indicates the predominance of **1a** in the source due to the stability of the *chair*-1,4-dioxane. For photoreactions, the C−O bond is found to be much more prone to rupture than the C−C bond due to the coordination of O to Mg^+ in the parent complexes. Photoreaction mechanisms are discussed in terms of two key insertion complexes, which rationalize all of the observed photoproducts.

Introduction

Photodissociation spectroscopy of M^+−molecules (M = metal atom) complexes provides useful information not only on the structures of the complexes but also on the energetics and dynamics of the reactions between M^+ and the molecules.[1−3] We have recently focused on the photoreactions of complexes between alkaline metal cations such as $Mg^{\bullet+}$ and organic molecules containing electronegative atoms, e.g., F, N, and O. The strategy consists of the electronic excitation of the unpaired electron of $Mg^{\bullet+}$, followed by the funneling of the electronic energy into the reaction channels involving the bond-breakage and bond-formation in the organic molecules. For example, by the photoexcitation of $Mg^{\bullet+}$ in $Mg^{\bullet+}$(multifluorinated benzenes), benzyne radical cations were produced by the loss of stable MgF_2.[4] Furthermore, interesting photochemistry has been revealed for $Mg^{\bullet+}$(2-fluoropyrdine). A facile fluorine migration step leads to the $FMg^+(C_5H_4N)$ intermediate, which accounts for all of the ring-opening photoproducts.[5] However, with further F-substitutions such as in $Mg^{\bullet+}$(2,6-di- and pentafluoropyrdine), very different photoreactions are observed although the initial fluorine migration step is similar.[6] For O-chelate complexes, e.g., $Mg^{\bullet+}(ROCH_2CH_2OR)$, H-shift reactions are induced by the photoexcitation of $Mg^{\bullet+}$, resulting in the formation of $Mg^{\bullet+}$-(H_2O), $Mg^{\bullet+}(CH_2O)$, and $Mg^{\bullet+}(HOCH_3)$ as major photoproducts through the rupture of the C−O bonds.[7]

Crown ether is an important class of molecules frequently appearing in molecular recognition and host−guest chemistry.[8−10] Interactions between crown ether and metal ions, especially alkaline metal ions, are central to biological processes, such as ion transport and enzyme catalysis. To do away with the influence of solvents and counterions in solution, a number of experiments have been performed in the gas phase to study complexations of crown ether with alkali metal ion.[11−24] Dearden and co-workers found that both ion size selection and macrocyclic effects play a role in the coordination of alkali metal cations into crown ethers.[11−15] Brodbelt et al. employed a kinetic method to study size selectivties of crown ethers toward alkali metal ions and found that for 15-crown-5, the selectivity order is $Li^+ \gg Na^+ > K^+ > Cs^+$.[16−19] Armentrout's group measured bond dissociation energies (BDEs) of M^+(12-crown-4) (M = Li, Cs), which vary from ∼0.90 eV for Cs^+ to 3.90 eV for Li^+,[20−23] in good agreement with a theoretical study.[24]

Conceptually, dioxanes can be regarded as crown ethers, i.e., 6-crown-2.[25] Therefore, photodissociation studies of alkaline metal cation−dioxanes complexes may help to understand the interaction of the metal cations with the lone pair electrons of oxygen in dioxanes as well as the reactions induced by the electronic excitation of the metal cations. To our knowledge, few such studies have been reported to date. Perhaps the closest work is about the adsorption and reaction of 1,4-dioxane on Pd (111),[25] in which the authors proposed a boat adsorption configuration with the lone pairs of the two oxygen atoms pointing toward the surface of Pd. In the present work, we have studied the photodissociation of the complexes of $Mg^{\bullet+}$-(dioxanes) in the gas phase using a laser time-of-flight reflectron mass spectrometer. Deuteration experiments and theoretical calculations have been performed to facilitate the identification of the reaction channels and the interpretation of the novel photoreactions.

* Address correspondence to these authors. E-mail: chsyang@ust.hk and wyguo@hdpu.edu.cn.

10.1021/jp060002r CCC: $33.50
Published on Web 03/10/2006

Methods

A. Experiments. The details about the photodissociation experiment have been described previously,[26] so only a brief introduction is presented here. A rotating magnesium rod (5 mm in diameter and 5 cm in length) was mounted 15 mm downstream from the exit of a pulsed valve (General Valve). Driven by a step motor, the sample rod rotated and translated simultaneously by a step motor on each laser pulse to expose fresh surfaces during the laser-ablation experiments. The pulsed valve was used to produce beams of the dioxane molecules by supersonic expansion of the vapor seeded in helium with a backing pressure of ~40 psi through a 0.5 mm diameter orifice. The second harmonic (532 nm) of a Nd:YAG laser (~40 mJ/pulse) was weakly focused on a ~1 mm diameter spot of the magnesium disk for the generation of metal cations. The laser-produced species containing metal ions and atoms traversed perpendicularly to the supersonic jet stream 20 mm from the ablation sample target, forming a series of metal cations solvated by dioxanes. The nascent complexes and clusters then traveled 14 cm downstream to the extraction region of the reflectron time-of-flight mass spectrometer (RTOFMS).

The cation−molecule complexes were accelerated vertically by a high voltage pulse in a two-stage extractor. All the cluster cations were reflected by the reflectron and finally detected by a dual-plate microchannel plate detector (MCP). For photodissociation experiments, a two-plate mass gate equipped with a high-voltage pulser was used to select desired cluster cations. The mass-selected cluster cations, once arriving at the turn-around region of the reflectron, were irradiated with a collimated beam of a dye laser for photolysis. The parent and nascent daughter cations were re-accelerated by the reflectron electric field, and detected by the MCP detector. The dye laser was pumped by a XeCl excimer laser (Lambda-Physik LPX210i/LPD3002). Laser dyes *p*-terphenyl, DMQ, BBQ, Stilbene 1, and Coumarin 440 were used to cover the spectral region of 335−450 nm, while the second harmonic with Coumarin 503 and Coumarin 480 covered the spectral region of 230−270 nm. The branching fractions of each fragment were obtained from the corresponding photodissociation difference mass spectra at different wavelengths.

B. Computations. Quantum mechanics calculations were performed with the GAUSSIAN 03 program.[27] The observed photoreactions, although initiated by the electronic excitation, were assumed to occur on the ground-state surface after internal conversion. All species involved were calculated by the density functional theory B3LYP method, using the 6-31+G** basis set.[28] Each stationary point was characterized by vibrational frequency analysis (minimum with zero; transition state with one imaginary frequency). To confirm the transition structures for some key reaction pathways, intrinsic reaction coordinate (IRC) calculations were used to follow the reaction pathways. All the relative energies are reported with the corrections of zero-point energy (ZPE). It should be cautioned that the use of the DFT/B3LYP method often encounters problems in dealing with radical cations.[29,30] Higher level calculations such as CCSD(T) would be desirable to get more accurate results. However, we did not resort to these more costly methods because the level of our calculations is sufficient to understand the reaction pathways based on the experimentally observed products.

The vertical excitation energies and corresponding oscillator strengths of the Mg^+−dioxane complexes were calculated by the TD-B3LYP/6-311++G** method based on the B3LYP/6-31+G** geometries.

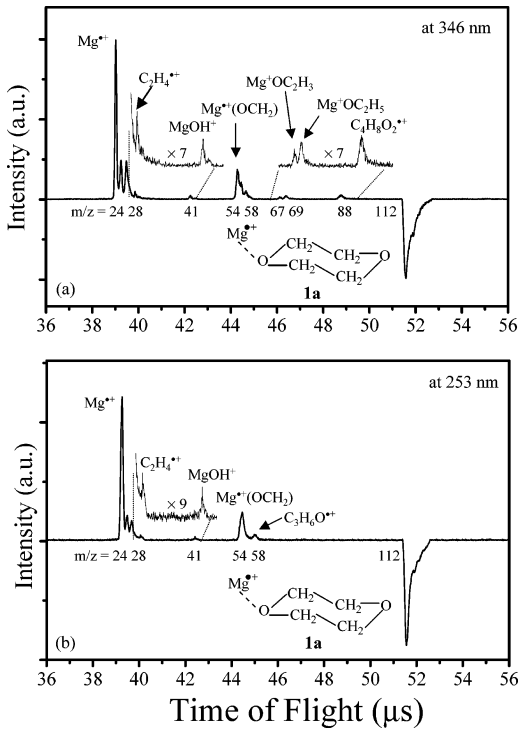

Figure 1. Photodissociation difference mass spectra of the complex $Mg^{\bullet+}$(1,4-dioxane) at 346 (a) and 253 nm (b).

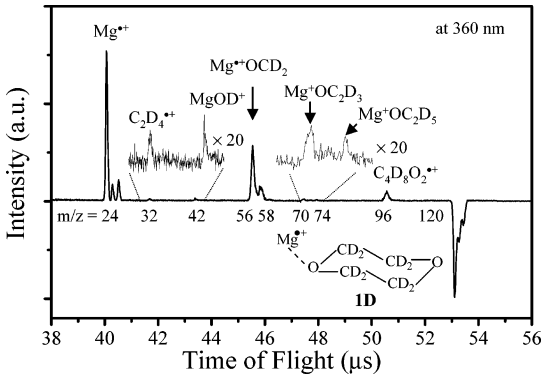

Figure 2. Photodissociation difference mass spectrum of the complex $Mg^{\bullet+}$(1,4-dioxane-d_8) at 360 nm.

Results and Discussion

A. Photoreaction Channels. We first examine the photodissociation difference mass spectra of $Mg^{\bullet+}$(1,4-dioxane) (**1**) in Figure 1 at long (a) and short (b) wavelengths. Some common photofragments are observed with *m*/*z* 24, 28, 41, 54, and 58 but additional peaks at *m*/*z* 67, 69, and 88 appear only in the long wavelength spectrum (346 nm). The dominant peak at *m*/*z* 24 can be easily assigned to $Mg^{\bullet+}$, which is generated from an evaporative process and from the subsequent evaporation from the photoproduct $Mg^{\bullet+}(O{=}CH_2)$. However, the assignment of other mass peaks needs more deliberation because the species with the same mass units may have different compositions and chemical formulas. In this regard, the corresponding isotope-labeled complex, $Mg^{\bullet+}$(1,4-dioxane-d_8) (**1D**), has been subjected to the same photodissociation experiment and the difference mass spectrum is shown in Figure 2. Clearly, the photofragment distribution of **1D** (Figure 2) is similar to that of **1** (Figure 1a) except for the difference in peak positions due to the deuteration. Careful analysis of the difference mass spectra has allowed the photoproduct structures to be determined as will be described below.

The intense photoproduct peak at *m*/*z* 54 in Figure 1a is found to shift up to *m*/*z* 56 in Figure 2, indicating the presence of two H atoms. Therefore, among the possible molecular formulas for *m*/*z* 54, i.e., $Mg^{\bullet+}(CH_2O)$, $C_3H_2O^{\bullet+}$, and $C_4H_6^{\bullet+}$, the last one can be ruled out. The species $C_3H_2O^{\bullet+}$ is rejected through chemical intuition because its formation is unfavorable; here as many as four C−H, C−C, and C−O bonds need to be broken. We are then left with $Mg^{\bullet+}(O{=}CH_2)$, which can be formed by the direct rupture of a C−O and a C−C bond in 1,4-dioxane, partnered by the neutral oxetane or formaldehyde and ethylene. Moreover, the isotopic character of the peak also indicates the presence of $Mg^{\bullet+}$ in the photoproduct.

Although no peak has been detected for **1D** that corresponds to the cation at *m*/*z* 58 for **1**, we can safely assign it to $C_3H_6O^{\bullet+}$ based on the fact that the cation of the same mass was also observed in the photodissociation of 1,4-dioxane radical cation in an ion cyclotron resonance (ICR) experiment.[31−33] By studying reaction patterns in D-labeled compounds, it was proven that $C_3H_6O^{\bullet+}$ has a chain-type structure ($\cdot CH_2{-}CH_2{-}O^+ = CH_2$) rather than a cyclic form.[31] The $C_3H_6O^{\bullet+}$ observed in our experiment is likely to have the same structure as the one mentioned above, i.e., $^{\bullet}CH_2{-}CH_2{-}O^+ = CH_2$. To continue, the photoproduct peaks at *m*/*z* 28/32 and 41/42 for **1**/**1D** can be readily ascribed to $C_2H_4^{\bullet+}/C_2D_4^{\bullet+}$ and $MgOH^+/MgOD^+$, respectively. Other possible species with the same *m*/*z* can be eliminated either by the mass discrepancy or unfavorable energetics and kinetics.

Finally, the one-to-one correspondence of the weak peaks at *m*/*z* 67, 69, and 88 for **1** (see Figure 1a) to the peaks at *m*/*z* 70, 74, and 96 for **1D** (see Figure 2) suggests that there are respectively 3, 5, and 8 hydrogen atoms in the photoproducts. Because there are at most eight hydrogen atoms in the parent complex, the *m*/*z* 88 photoproduct is obviously the 1,4-dioxane radical cation ($1,4\text{-}C_4H_8O_2^{\bullet+}$), which may be produced from a charge-transfer process. The other two photoproducts at *m*/*z* 67 and 69 are assigned to $Mg^+(-OCH{=}CH_2)$ and $Mg^+{-}OCH_2{-}CH_3$, respectively, which both arise from the rupture of the C−O bonds accompanied by hydrogen transfer.

We also studied the photodissociation of $Mg^{\bullet+}(1,3\text{-}C_4H_8O_2)$ (**1M**). Interestingly, only an intense peak at *m*/*z* 54 is detected other than the usually present $Mg^{\bullet+}$ peak at both long and short wavelengths, as shown in Figure 3. The peak at *m*/*z* 54 is believed to be $Mg^{\bullet+}(O{=}CH_2)$ by comparison with that from **1**. The simple photoreaction pattern and the high yield of the $Mg^{\bullet+}$-$(O{=}CH_2)$ photoproduct at long wavelength (Figure 3a) is believed to lie in the favorable structure of the complex of **1M**. Whereas the breaking of a C−C bond beside a C−O bond is necessary for the formation of $Mg^{\bullet+}(O{=}CH_2)$ from **1**, the photoproduct can be obtained from **1M** simply by the cleavage of two C−O bonds, which appears to be more facile. More detailed discussion about this issue will follow. The decrease of the yield of $Mg^{\bullet+}(O{=}CH_2)$ at short wavelength probably is due to its partial evaporative dissociation (Figure 3b).

B. Structures of the Parent Complexes and Some Photoproducts. The ground-state geometries of $Mg^{\bullet+}(1,4\text{-}C_4H_8O_2)$ (**1**) and its photofragments as well as $Mg^{\bullet+}(1,3\text{-}C_4H_8O_2)$ (**1M**) were optimized at the B3LYP/6-31+G** level. For energy calculations, the zero-point correction was taken into account. Moreover, for the comparison with the experimental action spectra, the TD-B3LYP/6-311++G** method was employed to calculate the absorption spectra of the selected isomers of **1**, using the ground-state geometries.

Figure 4 presents the optimized structures (with *chair* and *boat* configurations) of the complex $Mg^{\bullet+}(1,4\text{-}C_4H_8O_2)$ (**1a** and **1b**), $Mg^{\bullet+}(1,3\text{-}C_4H_8O_2)$ (**1M**), free 1,4-dioxane (**2a** and **2b**), and 1,4-dioxane radical cation (**3a** and **3b**). It should be noted that full optimizations of the *boat*-type $1,4\text{-}C_4H_8O_2$ and $1,4\text{-}C_4H_8O_2^{\bullet+}$ starting with a C_{2v} symmetry lead to C_2 geometries, which actually are not pure "*boat*" forms (see **2b** and **3b** in Figure 4). Nevertheless, we still reserve the terms of *chair* and *boat* for identifying the distinct structural differences between **2a**/**3a** and **2b**/**3b**. In the *chair* configuration of **1a**, $Mg^{\bullet+}$ is bonded to only

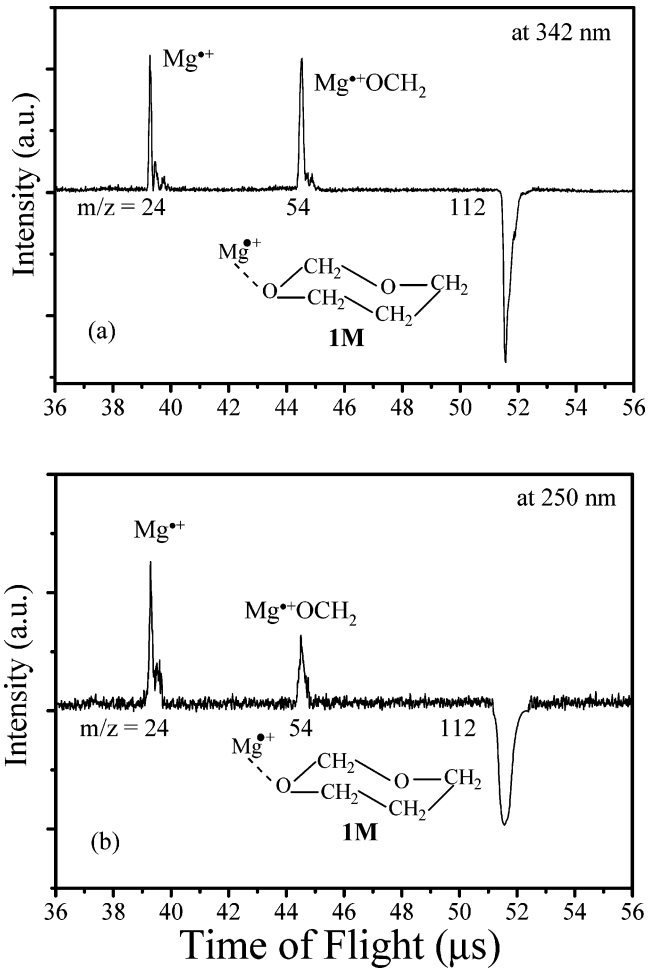

Figure 3. Photodissociation difference mass spectrum of the complex $Mg^{\bullet+}$(1,3-dioxane) at 342 (a) and 250 nm (b).

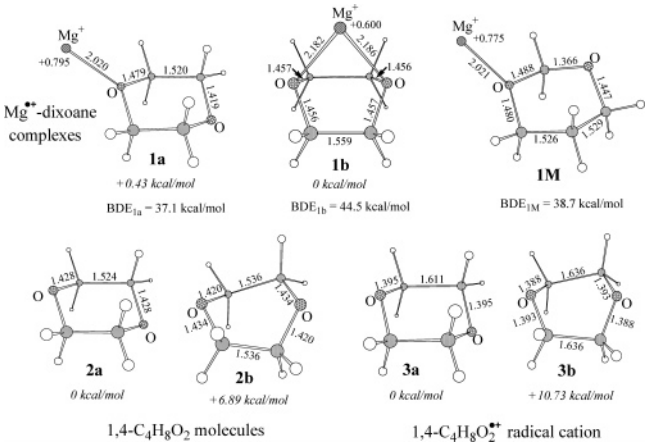

Figure 4. Calculated geometries of $Mg^{\bullet+}$(1,4-dioxane) (**1a** and **1b**), $Mg^{\bullet+}$(1,3-dioxane) (**1M**), molecules (**2a** and **2b**), and radical cations (**3a** and **3b**). The calculations are performed at the B3LYP/6-31+G** level. Bond lengths are in angstroms and BDE is bond dissociation energy.

one of the O atoms, whereas both of the O atoms can be coordinated to $Mg^{\bullet+}$ in the *boat* configuration of **1b**. As a result, the BDE of **1b** (44.5 kcal/mol) is found to be larger than that of **1a** (37.1 kcal/mol), which is close to the BDE of **1M** (38.7 kcal/mol). However, the energy of **1a** is merely 0.4 kcal/mol higher than that of **1b**. Comparatively, the energy difference between *chair* and *boat* configurations (**2a** and **2b**) of the 1,4-dioxane molecule is much larger (~6.90 kcal/mol), and even larger energy difference (~10.70 kcal/mol) is found for the corresponding radical cations (**3a** and **3b**). One of the consequences is that the *boat* configuration of 1,4-dioxane is absent or much more scarce in our nozzle source than the *chair* configuration. Although the coordination to $Mg^{\bullet+}$ can stabilize the *boat* configuration, **1b** is still difficult to form because (1) there are few *boat*-1,4-$C_4H_8O_2$ molecules to start with and (2) the *chair*-to-*boat* barrier may be too high for the association reaction of $Mg^{\bullet+}$ with *chair*-1,4-$C_4H_8O_2$. As will be shown below, this is supported by the comparison of the experimental action spectrum of the complex with the calculated absorption spectra of **1a** and **1b**.

It is noticed that substantial changes of geometries and charge distributions in the *chair*- and *boat*-1,4-$C_4H_8O_2$ have occurred upon coordination to $Mg^{\bullet+}$. For example, the four C−O bonds are equivalent in **2a** with a bond length of 1.428 Å, whereas two of them adjacent to $Mg^{\bullet+}$ in **1a** are stretched to 1.479 Å although the other two C−O bonds on the opposite side are nearly unaffected (see Figure 4). On the other hand, all of the C−O bonds in **1b** are lengthened by ~0.2−0.4 Å by the presence of $Mg^{\bullet+}$ in **2b**. Interestingly, the 1,4-$C_4H_8O_2$ molecule in **1b** is even closer to the *boat* configuration with C_{2v} symmetry than fully optimized **2b** due to the stabilizing effect of $Mg^{\bullet+}$. The $Mg^{\bullet+}$ attachment and the attendant charge transfer result in opposite changes of the C−O and C−C bond lengths in 1,4-$C_4H_8O_2$. It appears that the C−O bonds in the presence of $Mg^{\bullet+}$ tend to be activated. This is quite different from 1,4-$C_4H_8O_2^{\bullet+}$, in which the C−O bond is relatively intact and the likelihood of decomposition is low. Consequently, the formation of $C_2H_4^{\bullet+}$ accompanied by the rupture of two C−O bonds is likely to be from the reaction of 1,4-$C_4H_8O_2$ with the photoexcited $Mg^{\bullet+}$, rather than from a secondary decomposition of the charge-transfer photoproduct 1,4-$C_4H_8O_2^{\bullet+}$.

For **1M**, the two C−O bonds adjacent to $Mg^{\bullet+}$ are stretched to different extents due to the asymmetric presence of the other O atom. For example, the length of the C−O bond closer to the other O atom is stretched to as much as 1.488 Å. This bond appears to be more facile to rupture, which may provide an explanation of the intensive peak of $Mg^{\bullet+}(O{=}CH_2)$ from the photolysis of **1M**.

C. Action Spectra and Photofragment Branching Curves. Presented in Figure 5 are an action spectrum of $Mg^{\bullet+}$(1,4-$C_4H_8O_2$) (solid squares, 5a) and the corresponding photofragment branching fraction curves (5b) in the wavelength range of ~230−440 nm. In Figure 5a, the calculated absorption spectra for the *chair* and *boat* configurations of the complex (**1a** and **1b**) and CT action spectrum (open circles) are also shown for comparison. The action spectrum of $Mg^{\bullet+}$(1,4-$C_4H_8O_2$) consists of two main peaks that flank the atomic line of $Mg^{\bullet+}$ ($3^2P \leftarrow 3^2S$) at 280 nm. Clearly, the two peaks result from the splitting of the degenerate 3p orbitals of $Mg^{\bullet+}$ caused by the perturbation of 1,4-dioxane. On one hand, the p_z orbital of $Mg^{\bullet+}$ shifts up in energy because of its repulsive interaction with the lone pair electrons of the O atom. On the other hand, such repulsive interaction is minimized for the $p_{x,y}$ orbitals and further, the

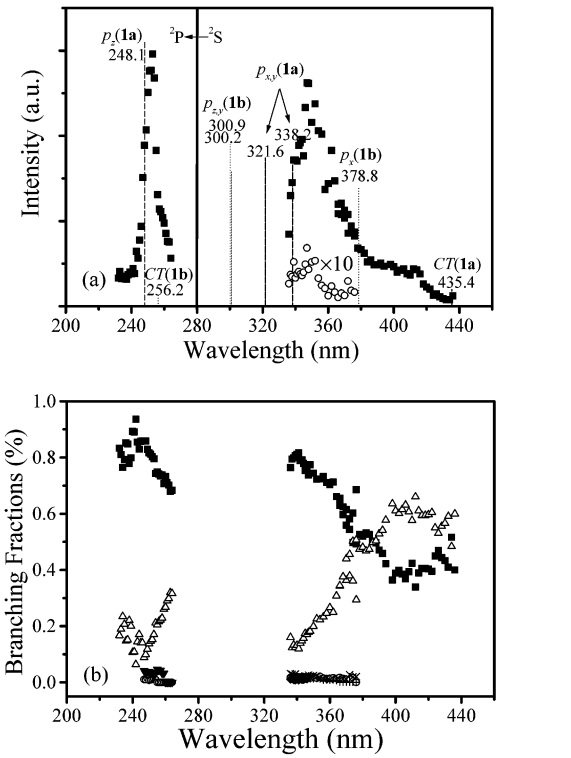

Figure 5. (a) Total yield action spectrum of $Mg^{\bullet+}$(1,4-dioxane) (solid squares) and CT action spectrum (open circles). The solid line indicates the atomic transition of $Mg^{\bullet+}$ ($3^2P \leftarrow 3^2S$) at 280 nm. The dashed lines denote the calculated absorption spectrum of $Mg^{\bullet+}$(*chair*-1,4-dioxane) (**1a**) while the dotted lines represent that of $Mg^{\bullet+}$(*boat*-1,4-dioxane) (**1b**). (b) Branching fraction curves of $Mg^{\bullet+}$(1,4-dioxane). For clarity, the labels for the photofragments other than $Mg^{\bullet+}$ and $Mg^{\bullet+}(O{=}CH_2)$ are omitted.

$p_{x,y}$ orbitals may interact attractively with the σ^* orbitals of the C−O bonds. Hence, the energies of the $p_{x,y}$ orbitals are lowered.

On inspection of the calculated absorption spectra of **1a** and **1b**, it is found that the former is in fairly good agreement with the experimental action spectrum. First, the 16.6 nm separation between the $P_{x,y}$ states explains the broadness of the red peak compared to the blue peak. In contrast, the separation between the $P_{x,y}$ states in the calculated absorption spectrum of **1b** is too large (78.6 nm) to account for the action spectrum. Second, the calculated $3P_z$ state of **1b** is also in the red side of the atomic line of $Mg^{\bullet+}$ ($3^2P \leftarrow 3^2S$) due to the bonding interaction of the $3p_z$ orbital in $Mg^{\bullet+}$ with the LUMO of *boat*-1,4-dioxane, which largely stabilizes the complex. Therefore the blue-shifted band cannot be explained with **1b**. On the other hand, the calculated absorption spectrum of **1a** shows both blue- and red-shifted bands in accord with the corresponding action spectrum. Last, the CT transition of **1b** is too high to explain the CT product observed in the long wavelength region (open circles in Figure 5a), whereas the position of the CT transition (435.4 nm) of **1a** accords well with the CT product. It appears that the $Mg^{\bullet+}$-(1,4-$C_4H_8O_2$) complex is indeed mostly produced in the *chair* configuration (**1a**) as concluded from our calculations above. Because **1a** is found to be the predominant configuration produced in our nozzle source, in what follows, it will be used for energetic and structural analyses of the photoreactions.

The photofragment branching fraction curves of the complex $Mg^{\bullet+}$(1,4-$C_4H_8O_2$) (Figure 5b) are dominated by the anti-correlation of $Mg^{\bullet+}(O{=}CH_2)$ with $Mg^{\bullet+}$. At λ > ~380 nm, the yield of $Mg^{\bullet+}(O{=}CH_2)$ is higher than that of $Mg^{\bullet+}$ but it decreases gradually from ~50% at 380 nm to < 20% at 330 nm. At the same time, the yield of $Mg^{\bullet+}$ varies in just the

SCHEME 1: Summary Diagram for the Observed Photoreactions of $Mg^{\bullet+}(1,4\text{-}C_4H_8O_2)$ (1a) along with the Calculated Reaction Energies (kcal/mol)

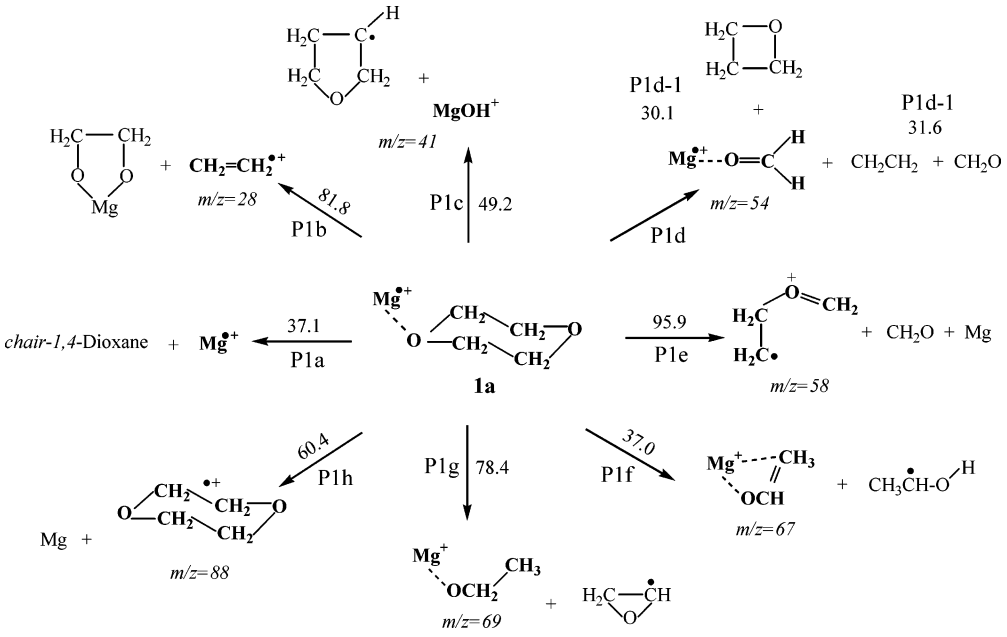

opposite way with the photolysis wavelength. This can be understood by the increasing decomposition of $Mg^{\bullet+}(O{=}CH_2)$ to $Mg^{\bullet+}$ with the decreasing wavelength. In the short-wavelength range (230−270 nm), although the photon energies (∼106.1−124.5 kcal/mol) are much higher than enough to completely evaporate $Mg^{\bullet+}$ from $Mg^{\bullet+}(O{=}CH_2)$, appreciable $Mg^{\bullet+}(O{=}CH_2)$ still survived. This is probably because (1) not all of the available energy has been deposited on the primary photoproduct and (2) the decomposition of $Mg^{\bullet+}(O{=}CH_2)$ is slow as a metastable decay at the time scale of the time-of-flight detection. The branching fractions of other fragment ions are all very low and nearly independent of the laser wavelengths (see labels other than solid squares and open triangles in Figure 5b).

D. Energetics and Mechanisms of the Photoreactions. The observed photoreactions of $Mg^{\bullet+}(1,4\text{-}C_4H_8O_2)$ (**1a**) are summarized in Scheme 1 along with the calculated reaction energies. As can be seen from Scheme 1, all the observed photoreactions except P1e are energetically accessible by a single one photon in the laser wavelength range we used. Although it was not possible to measure the laser-fluence dependence of the *m*/*z* 58 peak (corresponding to route P1e) due to its very low signal intensity, we tend to believe that the cations were produced from two-photon processes at the long wavelengths but only a single photon is needed in the short-wavelength range.

The most abundant photofragments of $Mg^{\bullet+}$ and $Mg^{\bullet+}(O{=}CH_2)$ come from routes P1a and P1d, which cost only 37.1 and ∼31 kcal mol^{-1}, respectively. As mentioned above, some of the $Mg^{\bullet+}$ photofragment comes from the decomposition of $Mg^{\bullet+}(O{=}CH_2)$, especially at the short wavelengths. However, the evaporative channel of the parent complex cannot be excluded, which could open after the internal conversion from the photoexcited states.[7]

The energy needed for the formation of the CT dissociation product ($C_4H_8O_2^{\bullet+}$) is calculated to be 60.4 kcal mol^{-1} (see route P1h), which is readily accessible by the photon energy in the wavelength range we have studied. The calculated oscillator strength for the CT transition (435.4 nm) is only 0.4% that of the $3P_x$-type excitation. Thus, we believe that $C_4H_8O_2^{\bullet+}$ was produced by the curve crossing from the $3P_{x,y}$-derived surfaces to the CT energy surface, followed by dissociation. The $3P_z$-derived surface may be too high in energy above the CT energy surface in the Franck−Condon region so that such curve-crossing is less likely. This may explain the absence of the CT product in the short-wavelength range.

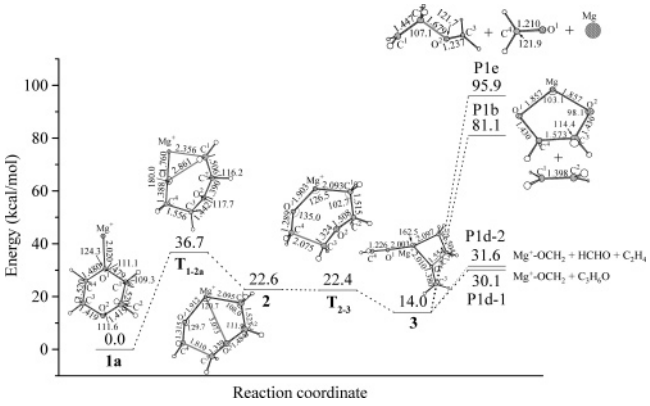

Figure 6. Schematic energy profiles for the formations of $Mg^{\bullet+}(O{=}CH_2)$, $Mg^{+}C_2H_4O_2$, and $C_3H_6O^{+}$ from $Mg^{\bullet+}$(1,4-dioxane) (**1a**) following the C−O activation. Bond lengths are in angstroms and bond angles are in degrees.

In the following, we will discuss the photoreactions in the $Mg^{\bullet+}$−dioxanes complexes in more detail.

*Formations of $Mg^{\bullet+}(O{=}CH_2)$ from **1a** and **1M**.* $Mg^{\bullet+}(O{=}CH_2)$ is a main photoproduct of $Mg^{+}(1,4\text{-}C_4H_8O_2)$ (**1a**) and an exclusive one of $Mg^{+}(1,3\text{-}C_4H_8O_2)$ (**1M**) (Figures 1 and 3). Intuitively, the photoreactions may proceed simply by breaking both the C^1−O^1 and the C^3−C^4 bonds in **1a** and both the C^1−O^1 and the C^2−O^2 bonds in **1M** following C−O activation, leading to the formation of oxetane or [ethylene + formaldehyde]. To unveil the mechanistic details of the C−O activation, we have theoretically investigated the reaction paths for both $Mg^{+}(1,4\text{-}C_4H_8O_2)$ (**1a**) and $Mg^{+}(1,3\text{-}C_4H_8O_2)$ (**1M**) at the B3LYP/6-31+G** level of theory. Depicted in Figures 6 and 7 are the calculated potential energy profiles for **1a** and **1M**. It should be pointed out that reaction pathways were searched on the ground state PES, since internal conversion from the excited sates to the ground state is expected to take place early (in the step of C−O activation) as mentioned above.

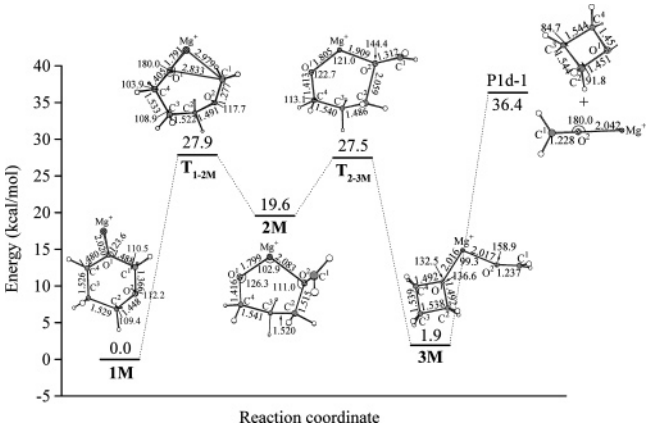

Figure 7. Schematic energy profile for the formation of $Mg^{\bullet+}(O{=}CH_2)$ from $Mg^{\bullet+}$(1,3-dioxane) (**1M**) following the C−O activation. Bond lengths are in angstroms and bond angles are in degrees.

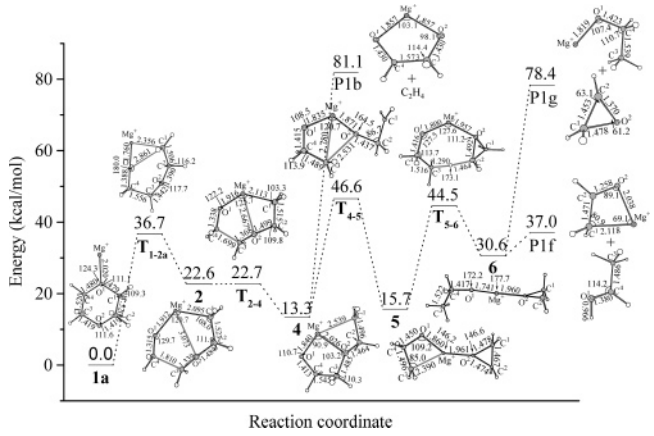

Figure 8. Schematic energy profiles for the formations of $Mg^+C_2H_4O_2$, $Mg^+OC_2H_5$, and $Mg^+OC_2H_3$ from $Mg^{\bullet+}$(1,4-dioxane) (**1a**) following the C−O activation. Bond lengths are in angstroms and bond angles are in degrees.

It can be seen from Figures 6 and 7 that insertion minimum (**2** or **2M**) can be formed by passing through $\mathbf{T_{1-2}}$ ($\mathbf{T_{1-2a}}$ or $\mathbf{T_{1-2M}}$) via Mg^+ insertion into the O^1-C^1 bond. The relative energies of the saddle points are calculated to be 36.7 and 27.9 kcal mol^{-1} for $\mathbf{T_{1-2a}}$ and $\mathbf{T_{1-2M}}$, respectively, suggesting the facility of the insertion process. This is especially the case for **1M** due to its weaker O^1-C^1 bond as revealed from the bond lengths (1.488/1.479 Å for **1M**/**1a**) as mentioned above. The different insertion abilities are also reflected in the photoproduct branchings ($Mg^{\bullet+}(O{=}CH_2)$) for the two complex systems (Figures 1 and 3). With the decrease in energy by 14.1 and 8.3 kcal mol^{-1}, the insertion minima (**2** and **2M**) are reached, respectively. The insertion minima are featured by seven-membered (**2**) and six-membered (**2M**) ring structures after breaking the C^1-O^1 bond of dioxanes and linking Mg^+ to C^1 and O^2, respectively (Figures 6 and 7). The stretched C^1-O^1 bonds may be effected by electron donation from the $3p_x$ or $3p_z$ orbital of Mg^{+}* to the σ_{CO}* orbital as well as from σ_{CO} to the 3s of Mg^{+}*, which is expected to proceed following the 3P-type excitations, since the interacting orbitals (i.e., 3p and σ_{CO}* as well as σ_{CO} and 3s) are parallel to each other to a certain extent. These electron donations also promote internal conversion of the excited sates ($3P_z$- and $3P_x$-types) to the ground state (3S-type) as revealed in a number of analogous systems.[4−7,34] One notices that the bond lengths of C^3-C^4 in **2** (1.810 Å) and C^2-O^2 in **2M** (1.515 Å) are extremely stretched, signifying considerable weakening of these bonds. The ultimate rupture of the weakened bonds is likely driven by the ring breathing vibration excited by the Mg^+ insertion into the C^1-O^1 bond and the sp hybridization at Mg^+, which tends to evolve toward a linear structure of $O-Mg-C^1(O^2)$. As a result, the insertion minima are rearranged to **3** and **3M** by passing through transition states $\mathbf{TS_{2-3}}$ and $\mathbf{TS_{2-3M}}$, respectively. The structures of these transition states exhibit much resemblance to those of the insertion minima (i.e., **2** and **2M**), insinuating early saddle points for the processes. It should be pointed out that although B3LYP/6-31+G** finds **2** to be a true minimum, ZPE effects place the complex slightly above $\mathbf{T_{2-3}}$.

In **3M**, the angle of the O−Mg−O part is 99.3°. This angle close to 90° is expected for complexes of Mg^+ with two closed-shell molecules.[26,34,35] Homolysis of the $(C_3H_6O)Mg^+-OCH_2$ bond yields oxetane and Mg^+OCH_2. The formation energy of Mg^+OCH_2 from **1M** is calculated to be 36.4 kcal/mol, which is within the photon energy we used and thus explains its formation in the experiments. On the other hand, **3** is featured by the linkage of Mg^+ to formaldehyde and chain-type structure of $CH_2CH_2OCH_2$ at the sites of the first C and O or two formaldehyde molecules and CH_2CH_2. This structure (**3**) is calculated to be 14.0 kcal mol^{-1} more unstable than **1a**. Homolysis of the Mg^+-C and Mg^+-O bonds of **3** yields products Mg^+OCH_2 and oxetane or formaldehyde + ethylene. The appearance energies of these two products are 30.1 and 31.6 kcal mol^{-1}, respectively. To wrap up, the different positions of the O atoms in dioxane result in different C−O insertion structures, which in turn lead to different reation patterns.

*Formations of $CH_2{=}CH_2^{\bullet+}$ (P1b) and $CH_2CH_2OCH_2^+$ (P1e) from **1a**.* **3** is also expected to be a precursor for $CH_2CH_2OCH_2^+$ and $C_2H_4^+$ by loss of Mg + CH_2O and *cyclo*-$Mg(OCH_2)_2$ with appearance energies of 81.8 and 95.9 kcal mol^{-1}, respectively (Figure 6). As mentioned above, **3M** has a structure characterized by linking Mg^+ to two stable molecules, i.e., formaldehyde and oxetane, thus the rupture of the Mg^+-oxetane bond leads exclusively to Mg^+-OCH_2 and oxetane. The difference in the structures of **3** and **3M** originates from the different positions of the two O atoms in their precursors **2** and **2M**. As we will discuss below, the C−O insertion minimum **2** may go through other channels such as P1b, P1f, and P1g following appreciable rearrangements of the seven-membered ring.

*Formations of $C_2H_4^+$ (P1b), $Mg^{\bullet+}(OCHCH_3)$ (P1f), and $Mg^{\bullet+}OCH_2CH_3$ (P1g) from **1a**.* To understand the mechanisms for the formation of these photoproducts, we traced the potential energy surface along the reaction pathways for the Mg^+(1,4-dioxane) (**1a**, Figure 4) system and the results are shown in Figure 8. When the insertion complex **2** is formed, certain ring vibrations may bring Mg^+ to the other O atom (O^2) in the formation of **4** by passing through $\mathbf{T_{2-4}}$. $\mathbf{T_{2-4}}$ is only 0.1 kcal mol^{-1} higher than **2**, indicating an early saddle point. In **4**, the Mg^+-C^1 bond (2.539 Å) is nearly broken, whereas the Mg^+-O^2 bond (2.026 Å) is strengthened, yielding a stable ($-Mg^+-O^1-C^4-C^3-O^2-$) five-membered ring structure. Heterolytic cleavage of the O^2-C^2 bond will produce P1b [$C_2H_2^+$ + ($-Mg-O-CH_2-CH_2-O-$)]. P1b is calculated to be endothermic by 81.1 kcal mol^{-1}, which is accessible in the long wavelength after taking account of thermal energies in the parent complexes.

Another exit of **4** is a ring-opening channel, which leads to the complex **5** by breaking the C^3-O^2 bond through the saddle point $\mathbf{T_{4-5}}$. The reaction barrier is calculated to be 33.3 kcal mol^{-1}. In **5**, Mg^+ is coordinated by two CH_2CH_2O groups but with different structures. This complex is 15.7 kcal mol^{-1} more unstable than the parent complex. With a H-shift from the

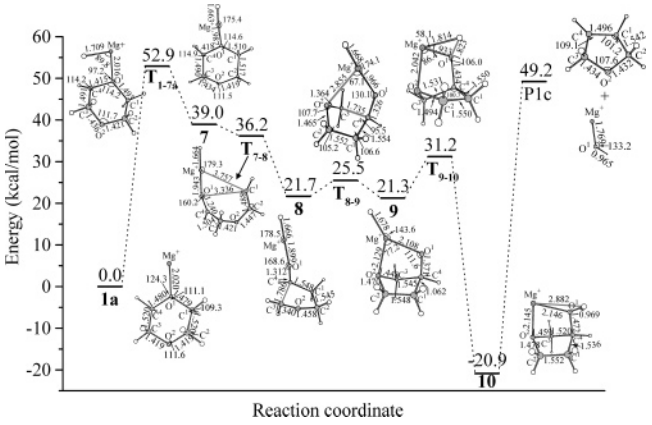

Figure 9. Schematic energy profiles for the formations of Mg^+OH from $Mg^{\bullet+}$(1,4-dioxane) (**1a)** following the C−H activation. Bond lengths are in angstroms and bond angles are in degrees.

ethylene oxide group to the end-C of the CH_2CH_2O group, the minimum **6** is reached via the transition state $\mathbf{T_{5-6}}$ with a barrier of only 28.8 kcal mol^{-1}. The direct breakage of the Mg^+-O^1 and Mg^+-O^2 bonds results in the formation of P1g ($Mg^+-OCH_2CH_3$) and P1f ($Mg^+(-OCHCH_2-)$), respectively. The overall reactions leading to the two products are endothermic by 78.4 and 37.0 kcal mol^{-1}, respctively, which are all accessible in the photon energy range of our experiments after taking account of thermal excitations in the dioxane complexes.

Formation of $Mg^{\bullet+}$*(OH) (P1c) from* ***1a****.* $Mg^{\bullet+}$(OH) is a minor photoproduct of **1a**, which can be produced at both long and short wavelengths. Figure 9 depicts the calculated potential energy profile for this photoreaction channel. To start with, Mg^+ abstracts a β-H to form **7** via $\mathbf{T_{1-7a}}$, which is located 52.9 kcal mol^{-1} above the parent complex, constituting the highest energy barrier along the whole reaction coordinate. In the minimum **7**, the $H-Mg^+-O^1$ group is nearly linear ($\angle HMgO^1 = 175.4°$), in accordance with a structure in which Mg^+ is coordinated by two open shell radicals.[34] It is noticed that the O^1-C^1 bond (1.51 Å) in **7** is stretched after the H-shift. This indicates the weakening and thus the activation of the C^1-O^1 bond.

Although the saddle point $\mathbf{T_{7-8}}$ is calculated to be 2.8 kcal mol^{-1} lower in energy than the precursor **7** owing to the zero-point effect (ZPE), it can be considered to be a genuine transition state connecting the minima **7** and **8** by checking the vibration vector of the imaginary mode, which indicates a facile process along the reaction coordinate. $\mathbf{T_{7-8}}$ has a triangular structure ($Mg^+O^1C^1$) and the C^1-O^1 bond length is calculated to be 3.336 Å, suggesting that the C^1-O^1 bond has almost been broken. After entering the minimum **8**, the active point C^1 binds to C^4 to form a five-membered ring connected by a $H-Mg^+-O^1-C^4$ linear chain group.

Assisted by the $C^4-O^1-Mg^+$ scissor vibration, Mg^+ binds to the O^2 atom by crossing a small barrier of 3.8 kcal mol^{-1} ($\mathbf{T_{8-9}}$), forming a crown structure **9**. This minimum is followed by a H-migration from Mg^+ to O^1 through a transition state structure $\mathbf{T_{9-10}}$. Consequently, a remarkably stable structure **10** is formed with two five-membered rings, which is even more stable than the parent complex by as much as 20.9 kcal mol^{-1}. This complex is in effect Mg^+(3-hydroxytetrahydrofuran) and because Mg^+ binds to two O atoms, it is expected to have a large binding energy. The direct cleavage of the Mg^+-O^2 and O^1-C^4 bonds brings in P1c (Mg^+OH + *cyclo*-OCH_2CH_2-$CHCH_2$) with an appearance energy of 49.2 kcal mol^{-1}. This provides an explanation for the *m*/*z* 41 peak in the mass spectrum in Figure 1.

Conclusion

The complexes of $Mg^{\bullet+}$ with two model cyclic ethers (1,4- and 1,3-dioxane) have been studied by the photodissociation technique coupled with time-of-flight mass spectrometry. A number of photoreaction channels from **1** and **1M** have been investigated and compared in the wavelength region of 230−440 nm. By using a fully deuterated 1,4-dioxane and with the help of density functional theory calculations, we are able to assign all of the observed photofragment peaks from **1**. Besides the most abundant photofragment $Mg^{\bullet+}$, the main photoproduct from **1** is found to be $Mg^{\bullet+}(O{=}CH_2)$. Other minor photoproducts are derived either from the $Mg^{\bullet+}$ insertion (e.g., $C_2H_4^{\bullet+}$, $MgOH^+$, $C_3H_6O^{\bullet+}$, $Mg^+OCH{=}CH_2$, and $Mg^+OCH_2CH_3$) or from the charge transfer (e.g., $C_4H_8O_2^{\bullet+}$). The low yields of these photoproducts are ascribed either to their higher formation energies or to the less favorable formation kinetics (complex processes). The photofragment distribution from **1M** is much simpler with only $Mg^{\bullet+}$ and $Mg^{\bullet+}(O{=}CH_2)$ being formed. The high yield and exclusive production of $Mg^{\bullet+}(O{=}CH_2)$ as a photoproduct are attributed to the six-membered ring structure of the insertion minimum **2M**, which simplifies the photoreaction pattern. By comparing the action spectrum and the calculated absorption spectra of candidate structures, we have shown that the *chair* form of the complex (**1a**) is predominant in our nozzle source. According to the theoretical calculations, one of the O atoms of *chair*-1,4-$C_4H_8O_2$ is coordinated to $Mg^{\bullet+}$ in the complex. By combining the experimental results and theoretical calculations, possible photoreaction mechanisms have been discussed. Specifically, the seven-membered -ring structure of the C−O insertion minimum from **1a** is able to rationalize all the observed photoproducts except that triggered by C−H activation. On the other hand, the six-membered-ring structure of the C−O insertion minimum from **1M** can only evolve into the complex of oxetane−Mg^+−formaldehyde, which leads ultimately to a single photoproduct of $Mg^+(O{=}CH_2)$. It is anticipated that this work contribute to the understanding of the reactive and nonreactive interactions of photoactivated metal cations with the simplest crown ether molecules.

Acknowledgment. We are grateful to the Research Grants Council of Hong Kong for financial support of this research. This work was supported by CNPC Innovation Fund and the Excellent Young Teachers Program and the Key Project (No. 104119) of MOE, PRC. We are also grateful for the financial support of the National Natural Science Foundation of China (Grant No. 20476061) and the China Petroleum & Chemical Corporation.

References and Notes

(1) Kleiber, P. D.; Chen, J. *Int. Rev. Phys. Chem.* **1998**, *17*, 1.
(2) Duncan, M. A. *Annu. Rev. Phys. Chem.* **1997**, *48*, 69.
(3) Yeh, C. S.; Pilgrim, J. S.; Willey, K. F.; Robbins, D. L.; Duncan, M. A. *Int. Rev. Phys. Chem.* **1994**, *17*, 231.
(4) Liu, H. C.; Wang, C. S.; Guo, W. Y.; Wu, Y. D.; Yang, S. H. *J. Am. Chem. Soc.* **2002**, *124*, 3794.
(5) Liu, H. C.; Yang, S. H.; Zhang, X. H.; Wu, Y. D. *J. Am. Chem. Soc.* **2003**, *125*, 12352.
(6) Wang, C. S.; Guo, W. Y.; Wu, Y. D.; Yang, S. H. In preparation.
(7) Liu, H. C.; Sun, J. L.; Yang, S. H. *J. Phys. Chem. A* **2003**, *107*, 5681.
(8) Vogtle, F.; Weber, E., Eds. *Host−Guest Complex Chemistry*: *Macrocycles*: *Synthesis, Structure, Applications*; Spring-Verlag: Berlin, Germany, 1985.
(9) Pedersen, C. J. *Science* **1988**, *241*, 536.
(10) Cram, D. J. *Science* **1988**, *240*, 760.
(11) Nicoll, J. B.; Dearden, D. V. *Int. J. Mass Spectrom.* **2001**, *204*, 171.

(12) Chu, I.-H.; Zhang, H.; Dearden, D. V. *J. Am. Chem. Soc.* **1993**, *115*, 5736.
(13) Dearden, D. V.; Zhang, H.; Chu, I.-H.; Wong, P.; Chen, Q. Z. *Pure Appl. Chem.* **1993**, *65*, 423.
(14) Zhang, H.; Dearden, D. V. *J. Am. Chem. Soc.* **1992**, *114*, 2754.
(15) Zhang, H.; Chu, I.-H.; Leming, S.; Dearden, D. V. *J. Am. Chem. Soc.* **1991**, *113*, 7415.
(16) Wu, H.-F.; Brodbelt, J. S. *J. Am. Chem. Soc.* **1994**, *116*, 6418.
(17) Brodbelt, J. S.; Liou, C.-C. *Pure Appl. Chem.* **1993**, *65*, 409.
(18) Maleknia, S.; Brodbelt, J. S. *J. Am. Chem. Soc.* **1992**, *114*, 4295.
(19) Liou, C.-C.; Brodbelt, J. S. *J. Am. Soc. Mass Spectrom.* **1992**, *3*, 543.
(20) More, M. B.; Ray, D.; Armentrout, P. B. *J. Phys. Chem. A* **1997**, *101*, 7007.
(21) More, M. B.; Ray, D.; Armentrout, P. B. *J. Phys. Chem. A* **1997**, *101*, 4254.
(22) More, M. B.; Ray, D.; Armentrout, P. B. *J. Phys. Chem. A* **1997**, *101*, 831.
(23) Ray, D.; Feller, D.; More, M. B.; Glendening, E. D.; Armentrout, P. B. *J. Phys. Chem.* **1996**, *100*, 16116.
(24) Hill, S. E.; Feller, D.; Glendening, E. D. *J. Phys. Chem. A* **1998**, *102*, 3813.
(25) Azad, S.; Bennett, D. W.; Tysoe, W. T. *Surf. Sci.* **2000**, *464*, 183.
(26) Yang, X.; Hu, Y. H.; Yang, S. H. *J. Phys. Chem. A* **2000**, *104*, 8496. Yang, X.; Liu, H. C.; Yang, S. H. *J. Chem. Phys.* **2000**, *113*, 3111. Yang, X.; Gao, K. L.; Liu, H. C.; Yang, S. H. *J. Chem. Phys.* **2000**, *112*, 10236.
(27) Frisch, M. J.; Trucks, G. W.; Schlegel, H. B.; Scuseria, G. E.; Robb, M. A.; Cheeseman, J. R.; Montgomery, J. A., Jr.; Vreven, T.; Kudin, K. N.; Burant, J. C.; Millam, J. M.; Iyengar, S. S.; Tomasi, J.; Barone, V.; Mennucci, B.; Cossi, M.; Scalmani, G.; Rega, N.; Petersson, G. A.; Nakatsuji, H.; Hada, M.; Ehara, M.; Toyota, K.; Fukuda, R.; Hasegawa, J.; Ishida, M.; Nakajima, T.; Honda, Y.; Kitao, O.; Nakai, H.; Klene, M.; Li, X.; Knox, J. E.; Hratchian, H. P.; Cross, J. B.; Adamo, C.; Jaramillo, J.; Gomperts, R.; Stratmann, R. E.; Yazyev, O.; Austin, A. J.; Cammi, R.; Pomelli, C.; Ochterski, J. W.; Ayala, P. Y.; Morokuma, K.; Voth, G. A.; Salvador, P.; Dannenberg, J. J.; Zakrzewski, V. G.; Dapprich, S.; Daniels, A. D.; Strain, M. C.; Farkas, O.; Malick, D. K.; Rabuck, A. D.; Raghavachari, K.; Foresman, J. B.; Ortiz, J. V.; Cui, Q.; Baboul, A. G.; Clifford, S.; Cioslowski, J.; Stefanov, B. B.; Liu, G.; Liashenko, A.; Piskorz, P.; Komaromi, I.; Martin, R. L.; Fox, D. J.; Keith, T.; Al-Laham, M. A.; Peng, C. Y.; Nanayakkara, A.; Challacombe, M.; Gill, P. M. W.; Johnson, B.; Chen, W.; Wong, M. W.; Gonzalez, C.; Pople, J. A. *Gaussian 03*, revision B.05; Gaussian, Inc.; Pittsburgh, PA, 2003.
(28) Becke, A. D. *J. Chem. Phys.* **1993**, *98*, 5648. Lee, C.; Yang, W.; Parra, R. G. *Phys. Rev. B* **1988**, *37*, 785.
(29) Bally, T.; Sastry, G. N. *J. Phys. Chem. A* **1997**, *101*, 7923. Crawford, T. D.; Kraka, E.; Stanton, J. F.; Cremer, D. *J. Chem. Phys.* **2001**, *114*, 10638. Braida, B.; Lauvergnat, D.; Hiberty, P. C. *J. Chem. Phys.* **2001**, *115*, 90. Koga, N.; Morokuma, K. *J. Am. Chem. Soc.* **1991**, *113*, 1907. Galbraith, J. M.; Schreiner, P. R.; Harris, N.; Wei, W.; Wittkopp, A.; Shaik, S. *Chem. Eur. J.* **2000**, *6*, 1446. Grafenstein, J.; Hjerpe, A. M.; Kraka, E.; Cremer, D. *J. Phys. Chem. A* **2000**, *104*, 1748. Kraka, E.; Anglada, J.; Hjerpe, A.; Filatov, M.; Cremer, D. *Chem. Phys. Lett.* **2001**, *348*, 115.
(30) Braïda, B.; Hazebroucq, S.; Hiberty, P. C. *J. Am. Chem. Soc.* **2002**, *124*, 2371. Hiberty, P. C.; Humbel, S.; Archirel, P. *J. Phys. Chem.* **1994**, *98*, 11697. Braïda, B.; Hiberty, P. C.; Savin, A. *J. Phys. Chem. A* **1998**, *102*, 7872. Braida, B.; Lauvergnat, D.; Hiberty, P. C. *J. Chem. Phys.* **2001**, *115*, 90.
(31) Baumann, B. C.; MacLeod, J. K.; Radom, L. *J. Am. Chem. Soc.* **1980**, *102*, 7928.
(32) Dunbar, R. C.; Huang, F.-S.; Klippenstein, S. J. *Int. J. Mass Spectrom. Ion Processes* **1993**, *128*, 21. Huang, F.-S.; Dunbar, R. C. *J. Am. Chem. Soc.* **1989**, *111*, 6497.
(33) Liu, H. C.; Hu, Y. H.; Yang, S. H.; Guo, W. Y.; Lu, X. Q.; Zhao, L. M. *Chem. Eur. J.* **2005**, *11*, 6392.
(34) Reddic, J. E.; Duncan, M. A. *J. Chem. Phys.* **1999**, *110*, 9948. Wesolowski, S. S.; Rollin, A. K.; Schaefer, H. F., III; Duncan, M. A. *J. Chem. Phys.* **2000**, *113*, 701.
(35) Sanekata, M.; Misaizu, F.; Fuke, F.; Iwata, S.; Hashimoto, K. *J. Am. Chem. Soc.* **1995**, *117*, 747. Watanabe, H.; Iwata, S.; Hashimoto, K.; Misaizu, F.; Fuke, K. *J. Am. Chem. Soc.* **1995**, *117*, 755.